CAN ONE MODALITY MODEL SYNERGIZE TRAINING OF OTHER MODALITY MODELS?

Anonymous authors
Paper under double-blind review

ABSTRACT

Learning with multiple modalities has recently demonstrated significant gains in many domains by maximizing the shared information across modalities. However, the current approaches strongly rely on high-quality paired datasets, which allow co-training from the paired labels from different modalities. In this context, we raise a pivotal question: *Can a model with one modality synergize the training of other models with the different modalities, even without the paired multimodal supervision?* Our answer is 'Yes'. As a figurative description, we argue that a writer, i.e., a language model, can promote the training of a painter, i.e., a visual model, even without the paired ground truth of text and image. We theoretically show that a superior representation can be achieved by the synergy between two different modalities, without paired supervision. As proofs of concept, we broadly confirm the considerable gains from the synergy across visual, language, and audio models. From a theoretical viewpoint, we first establish a mathematical foundation of the synergy between two different modality models, where each one is trained with its own modality. From a practical viewpoint, our work aims to broaden the scope of multimodal learning to encompass the synergistic usage of single-modality models, relieving a strong limitation of paired supervision.

1 INTRODUCTION

In recent years, *multimodal learning*, which aims to train the joint information across different modalities, is changing the paradigm of cutting-edge deep models from the conventional one modality training to the joint training of multiple modalities. Based on the recent success of large models, such as residual architectures (He et al., 2016), Transformers (Vaswani et al., 2017; Devlin et al., 2018; Liu et al., 2019) and Vision Transformers (ViT) (Dosovitskiy et al., 2021; Steiner et al., 2022), has spurred the emergence of numerous multimodal learning methods, mainly focusing on the vision-language domain.

Notable practices include CLIP (Radford et al., 2021) and ALBEF (Li et al., 2021), which pursue to align the representations from the vision and language modalities. Also, as another branch, CoOp (Zhou et al., 2022b) and CoCoOp (Zhou et al., 2022a) are based on adjustments of the prompt tokens of pretrained vision-language models. More recently, ViT+LLaMA (Pang et al., 2024) attempt to concatenate the pretrained language models with vision models, hypothesizing that the language models would filter significant information from the features extracted by the vision encoder.

This practical success relies on the presumption that the correlated modalities create a synergy when jointly trained on multimodal data samples, e.g., a synergy of the visual information and the textual description of an image, or a synergy of the RGB-based camera images and the LIDAR-based sensing signals of autonomous vehicles. As a theoretical foundation of the practices, researchers claim the existence of the true latent representations, which are able to encompass multiple modalities (Huang et al., 2021; Huh et al., 2024). This implies that when a paired supervision from multiple modalities is given, a model has the potential to more accurately represent the shared semantics by incorporating additional information from other modality models.

We want to raise a critical limitation of the prior works in both practical and theoretical sides. First, the existing multimodal learning methods mainly require the perfectly paired datasets, leading to the immense efforts in building multimodal datasets of high quality and restricting the usage of descent single-modality models in unleashing the synergy between modalities. Second, the current theory

only explains how multiple modalities promote better representations when paired labels across modalities are given.

In this context, we start by raising a pivotal question: *Can one modality model synergize training of other modality model, even without matched supervisions across modalities?* As an informal description of the question: Can a writer without true visual supervision (a language model), promote the training of a painter without true textual supervision, (a visual model)? Our answer is 'Yes'.

To showcase how one modality model promotes the training of the other models, we here provide a preliminary experiment, which is simple yet intuitive. We consider a case that a language model **[L]** synergizes the training of a visual model **[V]**; denoting it as **[L→V]** case. Specifically, a pretrained BERT model is used to promote the training of a ResNet model for the CIFAR-10 classification task (Krizhevsky et al., 2009). We used the text prompt `"This is about Class #."`, providing imperfect supervision loosely associated with the image. Herein, # indicates the Arabic class index, which does not provide semantic information of a given image. When utilizing this *imperfect* textual representation in training of the visual model, we surprisingly observe meaningful performance gains. As shown in Figure 1, when compared with the single-modality **[V]** case, our case **[L→V]** shows the well-clustered feature representations and accuracy gain[1]. Noteworthy, it demonstrates that language models help visual models, even with imperfect prompts, i.e., *a writer indeed helps a painter.* Our work aims to provide a theoretical foundation for understanding how it happens, and further proof-of-concepts in variety modalities, architectures, and tasks.

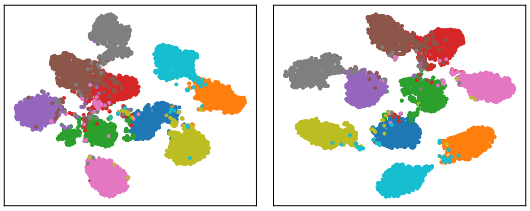

(a) **[V]** (Acc: 96.01) (b) **[L→V]** (Acc: 97.09)

Figure 1: t-SNE visualizations between single (left) and multimodality (right) on CIFAR-10

In this paper, we establish a theory that makes us envision how one modality promotes others without paired supervision. The key of this claim is that there exists an interpolated representation of two single-modality representations that outperforms the two (referred to **Theorem 1**). Furthermore, it can be well-approximated without paired supervisions from the given modalities (referred to **Theorem 2**). As the proof of concepts of our claim, we select the most widely-used modalities, i.e., vision **[V]**, language **[L]**, and audio **[A]**, to empirically evaluate the synergies between the three modalities. When using notation, $[M_i \rightarrow M_j]$, indicates that modality M_i promotes the training of modality M_j, we mainly confirm that language models promote the training of visual models, i.e., **[L→V]**. Moreover, we find that visual models or language models aid the training of audio models, and vice versa, i.e., **[V→A]**, **[A→V]**, **[L→A]** and **[A→L]**. Noteworthy, our theoretical claim is not limited to particular modalities, which broadens the fundamental understanding of the synergy between different modalities. Also, our work offers the opportunity to utilize the descent single-modality models to enhance other modality models, which strongly relieves the crucial demands of paired supervision of the current multimodal learning.

2 Related Works

2.1 Vision-Language Model

Vision and Language are among the most common modalities in deep learning, driving advancements in both empirical and theoretical perspectives. These developments led to foundation models like Transformers for language (Vaswani et al., 2017; Devlin et al., 2018; Liu et al., 2019) and Vision Transformer (ViT) for vision (Dosovitskiy et al., 2021; Steiner et al., 2022), enabling co-training with aligned datasets. A key example is CLIP (Radford et al., 2021), which contrastively learns latent features by maximizing similarity between matching vision-Language pairs while increasing separation for non-matching pairs. Building on this, methods have emerged that incorporate label spaces (Yang et al., 2022) or hard negative samples (Robinson et al., 2021; Li et al., 2021) to improve representation learning. However, these approaches require high-quality, perfectly aligned datasets.

[1]Full training details are described in Section 4

Our work overcomes this limitation by showing that even simplified or loosely aligned information can significantly enhance performance.

2.2 Translation of Language into Vision Modality

Recent advancements in vision-language foundation models have extended their applications across modalities. Large Language Models (LLMs), such as GPT-3 (Brown et al., 2020), BARD, and the LLaMA series (Touvron et al., 2023a;b; Dubey et al., 2024), have achieved state-of-the-art results in tasks like reasoning (Talmor et al., 2018) and knowledge retrieval (Kwiatkowski et al., 2019), primarily through prompt engineering. Building on this, several approaches have employed LLMs trained solely on language data to assist in vision tasks (Sharma et al., 2024), using their capabilities to generate new prompts or serve as auxiliary tools. Conversely, our approach focuses on utilizing latent features derived from language modality, even when imperfect data, without relying on the extensive capabilities of LLMs to perform vision-related tasks. This enables a more targeted and efficient use of cross-modal guidance.

2.3 Multimodal Learning

Several approaches have moved beyond vision-language paradigms to address a wider range of multimodal tasks, both empirically and theoretically. On the practical side, methods like MFAS and Multibench (Liang et al., 2021; Pérez-Rúa et al., 2019) employ fusion networks (Zadeh et al., 2017; Tsai et al., 2019) to combine inputs or latent features from multiple modalities, such as [Vison+Language] and [Vision+Audio], enhancing multimodal learning. Additionally, related research has explored handling missing or unpaired sets in multimodal. (Girdhar et al., 2023; Mizrahi et al., 2024; Lee et al., 2023; Kim & Kim, 2025). On the theoretical side, recent studies have shown that multimodal approaches can outperform unimodal by improving generalization bounds. (Huang et al., 2021; Bartlett & Mendelson, 2002; Li et al., 2018).

However, both empirical and theoretical perspectives share a few key limitation. From an empirical perspective, methods in fully supervised and unpaired modality settings often focus on improving multimodal model performance itself. In theoratical aspect, it emphasizes joint training to uncover broader shared latent spaces. However, synergy between modality models remains simultaneously underexplored from both empirical and theoretical sight. Thus, our approach addresses this gap by removing the need for paired supervision, promoting single-modality models to train others, and introducing a theoretical framework based on interpolated representations to explain their synergy.

3 Theoratical Perspective and Methods

3.1 Basic Notations and A Sketch of Mathematical Claims

Let us denote M_i and M_j as two different modalities. For inputs, let x^i and x^j indicate the paired inputs from modalties M_i and M_j respectively. In additon, $g_i : \mathcal{X}^i \to \mathcal{Z}^i$ and $g_j : \mathcal{X}^j \to \mathcal{Z}^j$ are two representation models that map an input to latent space, for the respective modalities. Also, $h_i : \mathcal{Z}^i \to \mathcal{Y}$ and $h_j : \mathcal{Z}^j \to \mathcal{Y}$ are hypotheses from embedding space to the label space $\mathcal{Y}$ for the respective modaltiy. Here, representations and hypotheses are independently trained on each modaltiy, without joint training.

In the context of multimodal learning, it is widely accepted to assume the existence of *true latent space* $\mathcal{Z}^\star$, which is the optimal representation across both modalities M_i and M_j (Huang et al., 2021). As a brief sketch, we show that there exists an interpolated latent representation space $\mathcal{Z}^k$ that shows smaller distance to $\mathcal{Z}^\star$, leading to outperform the two single-modality representations, i.e., $\mathcal{Z}^i$ and $\mathcal{Z}^j$ (referred to **Theorem** 1). It implies that we can find a better representation by interpolating two representations from different modalities. However, the first claim is limited in assuming correctly-paired inputs

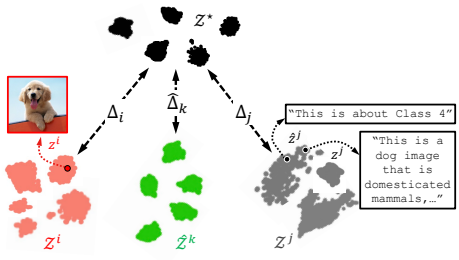

Figure 2: A conceptual sketch of our claims in **[L→V]** case

x^i and x^j, which draws extensive costs in annotations of multimodal learning. To this end, we argue that even given with an *imperfect* or *restricted* embedding $\hat{z}^j \in \hat{\mathcal{Z}}^j$ (not correctly-paired with z^i), there exists an interpolated representation $\hat{\mathcal{Z}}^k$ between $\mathcal{Z}^i$ and $\hat{\mathcal{Z}}^j$, which is closer to the true representation, leading to surpass the two, i.e., $\mathcal{Z}^i$ and $\mathcal{Z}^j$ (referred to **Theorem** 2). Fig. 2 illustrates a brief sketch of our claims. It means that imperfect samples from modality M_j can promote the training of the superior representation that promotes the performance of modality M_i; enabling the $[M_j \rightarrow M_i]$ case. In the following part, we provide the formal description.

3.2 How One Modality Model Synergize the Training of Others?

We begin by introducing the distance metric between two distributions $\mathcal{P}_1$ and $\mathcal{P}_2$ as follows:

Definition 1 (2-Wasserstein Distance (Villani et al., 2009))**.** *2-Wasserstein distance between 2 distribution $\mathcal{P}_1$ and $\mathcal{P}_2$ is defined as:*

$$W_2(\mathcal{P}_1, \mathcal{P}_2) = \inf_{\gamma \in \Gamma(\mathcal{P}_1, \mathcal{P}_2)} \left(\int_{\mathcal{Z}^1 \times \mathcal{Z}^2} d(z_1, z_2)^2 d\gamma(z_1, z_2) \right)^{1/2} \tag{1}$$

where $\Gamma(\mathcal{P}_1, \mathcal{P}_2)$ is all set of joint distribution (couplings) of $\mathcal{P}_1$ and $\mathcal{P}_2$.

We use 2-Wasserstein Distance to represent the distance between the probability density functions of the extracted features from different representations, as described below:

Definition 2. *Let $z^i \in \mathcal{Z}^i$, $z^j \in \mathcal{Z}^j$, and $z^\star \in \mathcal{Z}^\star$ denote the latent spaces of the i,j-modality, and the true latent space, where $z^\star$ represents the optimal representation across both modalities. z^i and z^j are assumed to be correctly-paired, which means that they represent the same underlying concept but in different modalities (e.g., i for image and j for text). Furthermore, let $\mathcal{P}_i$, $\mathcal{P}_j$, and $\mathcal{P}_\star$ are their corresponding distributions, i.e., $z^i \sim \mathcal{P}_i(z^i|x^i)$, $z^j \sim \mathcal{P}_j(z^j|x^j)$, and $z^\star \sim \mathcal{P}_\star(z^\star)$. The distances between the distributions are then defined as follows:*

$$\Delta_i := W_2(\mathcal{P}_\star, \mathcal{P}_i), \quad \Delta_j := W_2(\mathcal{P}_\star, \mathcal{P}_j) \quad \textit{and} \quad \Delta_{ij} := W_2(\mathcal{P}_i, \mathcal{P}_j), \tag{2}$$

where Δ_i, Δ_j, and Δ_{ij} are positive real numbers.

Let us define an interpolated representation between the representations of two different modalities:

Definition 3. *Let latent space $z^k \in \mathcal{Z}^k$ is an interpolated representation between the latent representation spaces of the i,j-modalities with interpolation coefficient $\alpha \in [0, 1]$, as follows:*

$$\mathcal{Z}^k := \{z^k = (1-\alpha)z^i + \alpha z^j \mid z^i \in \mathcal{Z}^i, z^j \in \mathcal{Z}^j\}. \tag{3}$$

In addition, let $\mathcal{P}_k$ denote the distribution of z^k, and 2-Wasserstein distance between $\mathcal{P}_k$ and $\mathcal{P}_\star$ is $\Delta_k := W_2(\mathcal{P}_\star, \mathcal{P}_k)$.

Assumption 1. *Let Δ_{ij} not converge to 0, i.e., $\Delta_{ij} \gg 0$.*

Assumption 1 implies that even if modalities M_i and M_j are similarly distant from the true latent space, the distance between M_i and M_j remains significant. Intuitively, while two modalities may represent similar information in certain contexts, their overall representations can differ markedly. Furthermore, they may contain distinct information. For example, modality **[L]** can effectively convey representations about "questions," whereas modality **[V]** may hard to provide such representations. Thus, assuming that $\Delta_{ij} \gg 0$ is a reasonable and justifiable consideration.

In the following theorem, we present the closed form solution of the interpolation coefficient α^*, which makes $\mathcal{Z}^k$ be closest to $\mathcal{Z}^\star$.

Theorem 1. *The optimal α^* that minimizes Δ_k is formulated as follows:*

$$\alpha^* = \frac{\Delta_i^2 - \Delta_j^2 + \Delta_{ij}^2}{2\Delta_{ij}^2} \tag{4}$$

Moreover, the resulting interpolated representation satisfies $\Delta_k \leq \Delta_i$ and $\Delta_k \leq \Delta_j$.

Corollary 1.1. *The optimal α^* is bounded as follows:*

$$\alpha^* = \begin{cases} \left[\dfrac{\Delta_i}{\Delta_i + \Delta_j}, 1 \right] & \text{if } \Delta_i > \Delta_j \\ \left[0, \dfrac{\Delta_i}{\Delta_i + \Delta_j} \right] & \text{otherwise} \end{cases} \tag{5}$$

For the proofs of Theorem 1 and Corollary 1.1, please see Appendix A.2.

Remark 1.1. ***(The behavior of α^*)*** *α^* is strongly influenced by the quality of modalities. For an instance, let us discuss what happens when Δ_j changes while fixing Δ_i. Specifically,* ***1)*** *when $\Delta_i > \Delta_j$, i.e., modaltiy M_j is superior to modality M_i, the optimal α^* will be greater than 0.5, i.e., $\alpha^* > 0.5$, implying that $\mathcal{P}_k$ tends to be closer to $\mathcal{P}_j$. Conversely,* ***2)*** *if $\Delta_i < \Delta_j$, $\alpha^* < 0.5$, indicating that $\mathcal{P}_k$ shifts closer to $\mathcal{P}_i$. Finally,* ***3)*** *when $\Delta_i = \Delta_j$, the optimal α^* equals to 0.5. It is convincing that the behavior of α^* shows that the superior interpolated representation forms near to the better modality. Further discussions are provided at Appendix A.2.*

Remark 1.2. ***(The condition of the synergy)*** *For a scenario of utilizing M_j in training M_i, it is crucial to judge how beneficial M_j is in promoting the training of the M_i. If modality M_j does not bear information on the true latent space, where $\Delta_j \gg \Delta_i$, this suggests that the M_j is much far from both the true latent space and the M_i. Thus, leveraging M_j is not effective in training M_i, and it makes to α^* close to 0, which leads to the single-modality training of M_i. Thus, Assumption 1 is critical to ensure that information from the M_j can be effectively utilized.*

As aforementioned, obtaining exactly paired datasets in real-world scenarios is challenging. Theorem 1 assumes the perfectly matched pairing of z_i and z_j with a common concept. Let us draws a setting of 'imperfect' or 'restricted' pairing between modalities into our theoretical framework.

Definition 4. *Let $\hat{z}^j \in \hat{\mathcal{Z}}^j$ be the imperfect latent space of the j-modality, with $\hat{\mathcal{P}}_j$ as its corresponding distribution. The gap δ between z^j and $\hat{z}^j$ is defined as:*

$$\delta := W_2(\mathcal{P}_j, \hat{\mathcal{P}}_j). \tag{6}$$

Additionally, the distance from $\hat{\mathcal{P}}_j$ to the true latent space $\mathcal{P}_\star$ and $\mathcal{P}_i$ are denoted as respectively:

$$\hat{\Delta}_j := W_2(\mathcal{P}_\star, \hat{\mathcal{P}}_j) \quad \text{and} \quad \hat{\Delta}_{ij} := W_2(\mathcal{P}_i, \hat{\mathcal{P}}_j). \tag{7}$$

Based on Definition 3 of imperfect representation, we rephrase the Theorem 1 to provide the following theorem:

Theorem 2. *Let $\hat{z}^k \in \hat{\mathcal{Z}}^k$ be the interpolated latent space between the M_i and the restricted M_j, defined by the interpolation coefficient α as: $\hat{\mathcal{Z}}^k = \{\hat{z}^k = (1-\alpha)z^i + \alpha\hat{z}^j \mid z^i \in \mathcal{Z}^i, \hat{z}^j \in \hat{\mathcal{Z}}^j\}$, where $\hat{\mathcal{P}}_k$ represents its distribution. Let the 2-Wasserstein distance between $\hat{\mathcal{P}}_k$ and $\mathcal{P}_\star$ be denoted as $W_2(\mathcal{P}_\star, \hat{\mathcal{P}}_k) = \hat{\Delta}_k$. Then the optimal $\hat{\alpha}^*$ that minimizes $\hat{\Delta}_k$ is formulated as follows: $\hat{\Delta}_k$:*

$$\hat{\alpha}^* = \frac{\Delta_i^2 - \hat{\Delta}_j^2 + \hat{\Delta}_{ij}^2}{2\hat{\Delta}_{ij}^2} \tag{8}$$

Moreover, the resulting interpolated representation satisfies $\hat{\Delta}_k \leq \Delta_i$ and $\hat{\Delta}_k \leq \hat{\Delta}_j$.

Corollary 2.1. *The optimal $\hat{\alpha}^*$ is bounded as follows:*

$$\hat{\alpha}^* = \begin{cases} \left[\dfrac{\Delta_i}{\Delta_i + \Delta_j + \delta}, 1 \right] & \text{if } \Delta_i > \hat{\Delta}_j \\ \left[0, \dfrac{\Delta_i}{\Delta_i + \Delta_j} \right] & \text{otherwise} \end{cases} \tag{9}$$

For the proofs of Theorem 2 and Corollary 2.1, please see Appendix A.3.

Remark 2.1. *(δ **does not hinder the synergy**) Although $\hat{z}^j \sim \hat{\mathcal{P}}_j$ deviates from $\mathcal{P}_j$, it still represents the latent space of the M_j. We can extract an imperfect feature representation from $\mathcal{P}_j$ by giving imperfect input to the modality M_j. This allows $\hat{z}^j$ exist in the distribution $\mathcal{P}_j$[2]. Consequently, $\hat{z}^j$ is closer to or part of the latent space of the M_j than to that of the M_i or the true latent space. Therefore, additional gap δ in Equation 6 is unlikely to significantly impact the determination of the optimal $\hat{\alpha}^*$, as δ will be much smaller than both Δ_i and Δ_j. It stems for δ does not hinder the synergy between two modalities, i.e., the modality M_j can promote the training of M_i, even with an imperfect representation.*

Remark 2.2. *(M_j **indeed helps the training of** M_i) In training M_j, we can find a superior representation $\hat{\mathcal{Z}}^k$ by utilizing imperfect feature representation from M_j. When revisiting the conceptual sketch in Fig. 2 and the preliminary experiments on CIFAR-10 shown in the Introduction, an imperfect textual description, i.e., `"This is about Class #."` works as $\hat{z}^j$ promotes the training of visual models by finding the interpolated representation.*

3.3 Methodology: Training Modality M_i by leveraging Modality M_j

Based on our theory, we thus propose a training method for one modality M_i by leveraging modality M_j with sampling imperfect $\hat{z}_j$ from the representation space of M_j. Let us consider the scenario for training modality M_i by leveraging modality M_j, i.e., $[M_j \rightarrow M_i]$, without loss of generality.

We extend our notation by introducing an uppercase superscript to denote the data modality. Specifically, let $\mathcal{S}^i = \{(\mathbf{x}^i_m, y^i_m)\}_{m=1}^M$, representing the dataset for the M_i to be learned, where $\mathbf{x}^i_m$ denotes the input data and y^i_m its corresponding label, where M is the number of data points sampled. Similarly, let $\mathcal{S}^j = \{\hat{\mathbf{x}}^j_m\}_{m=1}^M$ represent the sampled set of imperfect samples of the M_j. This yields the latent vectors $\hat{z}^j_m = g_j(\hat{\mathbf{x}}^j_m) \in \hat{\mathcal{Z}}^j$, as introduced in Definition 4, where $g_j(\cdot)$ is the pretrained model function associated with the M_j. $\mathcal{S}^i$ and $\mathcal{S}^j$ are sampled subsets from their respective full modality datasets, $\mathcal{D}^i$ and $\mathcal{D}^j$. In last, the primary objective is to minimize risk through Empirical Risk Minimization (ERM). We then define two associated empirical risks by the following loss functions:

$$\text{Classification Loss: } \mathcal{L}_{cls} = \mathop{\mathbb{E}}_{(\mathbf{x}^i_m, y^i_m)\sim\mathcal{S}^i} \left[\mathcal{L}_{CE}(h \circ g(\mathbf{x}^i_m), y^i_m)\right]$$

$$\text{Latent Loss: } \mathcal{L}_z = \mathop{\mathbb{E}}_{(\mathbf{x}^i_m, y^i_m, \hat{z}^j_m)\sim\mathcal{S}^i\times\hat{\mathcal{Z}}^j} \left[\frac{1}{2}||g(\mathbf{x}^i_m) - \hat{z}^j_m||^2\right]$$

In this approach, the classification loss $\mathcal{L}_{cls}$ is utilized to optimize the learning of the M_i while latent loss $\mathcal{L}_z$ is treated as regularization term, enforcing alignment of features from the M_j. We scaled $\mathcal{L}_z$ by a factor of $1/2$, to facilitate $g(\mathbf{x}^i_m)$ in following $\hat{z}^j_m$, thereby eliminating additional multiplication term at the front of $\mathcal{L}_z$ during backpropagation.

We here propose a straightforward loss formulation, which allows to find the interpolated representations between two modalities. We linearly combine the classification and latent lose terms: $\mathcal{L}_{total} = (1-\alpha)\mathcal{L}_{cls} + \alpha\mathcal{L}_z$. A pseudocode of the learning procedures is given in Appendix B.2. In the following section, we describe how to obtain imperfect feature $\hat{z}^j$ for each modality, including vision, language, and audio.

4 Experimental Results

In this section, we provide an overview of the experimental results, along with detailed descriptions of the datasets, models and additional experimental settings.

4.1 Experimental Settings

Datasets For the main experiments, we test on the ImageNet-1K dataset (Krizhevsky et al., 2012) for visual tasks as the case of **[L→V]**. For further experiments in the multimodal setting, we employ the IEMOCAP (Busso et al., 2008) and AVMNIST (Liang et al., 2021; Li et al., 2023) datasets.

[2]We fully describe how it can be done in the empirical testing in Section 4 and Appendix B.

Table 1: Classification results on ImageNet-1K and evaluation benchmarks (OOD and robustness)

Model [L→V]	IN	V2	Rend.	Sketch	A	Style.	C (↓)
ResNet-50 (reproduced)	74.97	63.06	36.28	24.35	3.99	8.11	70.96
+ BERT (Devlin et al., 2018)	76.25	65.03	38.27	26.47	5.27	9.4	68.84
+ **RoBERTa** (Liu et al., 2019)	**76.90**	**65.89**	**38.75**	**26.70**	**5.36**	**10.11**	**67.35**
ViT-B/32 (reproduced)	72.39	58.07	35.51	23.12	7.24	13.39	59.82
+ BERT (Devlin et al., 2018)	74.33	60.99	36.47	25.21	8.13	14.83	57.33
+ **RoBERTa** (Liu et al., 2019)	**74.92**	**61.76**	**37.93**	**25.91**	**9.10**	**15.27**	**56.66**
ViT-B/16 (reproduced)	77.98	65.57	37.62	25.66	15.20	13.93	57.22
+ BERT (Devlin et al., 2018)	79.22	66.72	38.25	26.74	17.32	15.04	55.52
+ **RoBERTa** (Liu et al., 2019)	**79.58**	**67.90**	**39.15**	**27.91**	**19.73**	**15.44**	**54.55**

Table 2: Classification results on IEMOCAP and AVMNIST datasets on each cases of $[M_j \rightarrow M_i]$.

Datasets	Model [L→A]	Accuracy	Model [A→L]	Accuracy
IEMOCAP††	Wav2Vec2† (Ravanelli et al., 2021)	59.46	BERT (Devlin et al., 2018)	55.81
	+ BERT-B (Devlin et al., 2018)	60.44	**+ Wav2Vec2-B** (Baevski et al., 2020)	**56.49**
	+ **BERT-L** (Devlin et al., 2018)	**61.20**	+ Wav2Vec2-L (Baevski et al., 2020)	56.05
Datasets	**Model [V→A]**	**Accuracy**	**Model [A→V]***	**Accuracy**
AVMNIST	Audio Model (Li et al., 2023)	41.28	Vision Model (Li et al., 2023)	65.18
	+ **ResNet-18** (He et al., 2016)	42.08	+ Wav2Vec2-B (Baevski et al., 2020)	66.37
	+ **ResNet-34** (He et al., 2016)	**42.44**	+ **Wav2Vec2-L** (Baevski et al., 2020)	**66.69**

†: SpeechBrain (Ravanelli et al., 2021) experimented with 4 out of 6 labels; we used the all labels.
††: Since transformer-style model requires numerous data, we fine-tuned the pretrained model.
*: Since the audio data in AVMNIST is based on spectrograms, we use the original raw audio data prior to its conversion into spectrogram.

IEMOCAP includes [A+L+Video] modalities, where we specifically focus on the [A+L] subset for our experiments. We performed experiemnts on both direction, **[L→A]** and **[A→L]**. For AVMNIST, which contains [A+V] modalities, we followed the preprocessing steps outlined in CentralNet (Vielzeuf et al., 2018), transforming raw audio into 112×112 spectrograms and utilizing 28×28 PCA-projected MNIST images. Similar to IEMOCAP datasets, we conducted experiments in both directions, **[V→A]** and **[A→V]**.

Models For the **[L→V]** case with the ImageNet-1K dataset, we employed modern architectures, including ResNet50 (He et al., 2016), ViT-B/32, and ViT-B/16 for **[V]** modality. To incorporate additional information from text prompts, we utilized pretrained BERT (Devlin et al., 2018) and RoBERTa (Liu et al., 2019), two extensively used transformer encoders for embedding the **[L]** modality. We use the "large" size versions on both encoders. For the **[L→A]** and **[A→L]** cases with IEMOCAP datasets, we employed a Wav2Vec2 (Baevski et al., 2020) model with SpeechBrain (Ravanelli et al., 2021) configurations for **[A]** modality, alongside pretrained BERT-B and BERT-L for the **[L]** modality. For the **[V→A]** case with AVMNIST experiments, we used the audio encoder from AGM (Li et al., 2023), enhanced with an additional classification layer for the **[A]** modality, and a pretrained ResNet-18 for the **[V]** modality. In addition, for the **[A→V]** case with AVMNIST, we used the original pretrained Wav2Vec2-B/L model for the **[A]** modality. Especially, in Table 2, "-B" refers to "base" size of model, while "-L" refers to "large" size configuration. For $[M_j \rightarrow M_i]$, all model parameters of M_j modality are frozen.

Additional Settings *(how to get $\hat{z}^j$)* For the **[L→V]** case with the ImageNet-1K dataset, we obtain $\hat{z}^j$ by employing simple prompt engineering that provides imperfect and restricted information for the language modality. Specifically, prompts like `"This is about Class #."` are used, where # is a random number unrelated to the actual class label, ensuring imperfect supervision for the language modality. For the **[L→A]** case with IEMOCAP, $\hat{z}^j$ is generated using prompts like `"This is about Emotion #."`, where # is also a random number unrelated to actual labels, helping audio classification on the IEMOCAP dataset. We exclude the paired **[L]** modality data in IEMOCAP. In the **[A→L]** case with IEMOCAP, we added Gaussian noise to audio data and

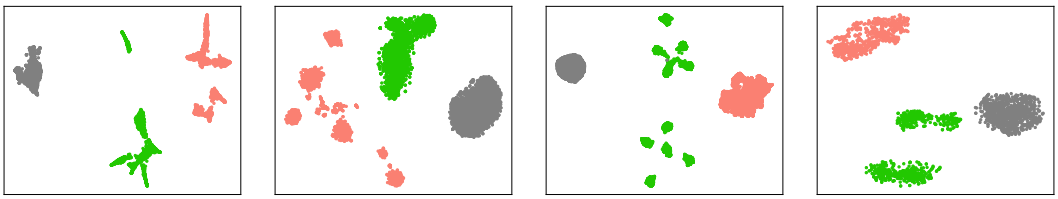

IEMO. [L→A]	WD	IEMO. [A→L]	WD	AVMN. [V→A]	WD	AVMN. [A→V]	WD
$W_2(\mathcal{P}_A, \hat{\mathcal{P}}_k)$	0.494	$W_2(\mathcal{P}_L, \hat{\mathcal{P}}_k)$	0.965	$W_2(\mathcal{P}_A, \hat{\mathcal{P}}_k)$	0.025	$W_2(\mathcal{P}_V, \hat{\mathcal{P}}_k)$	0.908
$W_2(\mathcal{P}_L, \hat{\mathcal{P}}_k)$	0.141	$W_2(\mathcal{P}_A, \hat{\mathcal{P}}_k)$	0.460	$W_2(\mathcal{P}_V, \hat{\mathcal{P}}_k)$	0.754	$W_2(\mathcal{P}_A, \hat{\mathcal{P}}_k)$	0.502
$W_2(\mathcal{P}_A, \mathcal{P}_L)$	**0.977**	$W_2(\mathcal{P}_L, \mathcal{P}_A)$	**1.005**	$W_2(\mathcal{P}_A, \mathcal{P}_V)$	**0.790**	$W_2(\mathcal{P}_V, \mathcal{P}_A)$	**0.954**

Figure 3: t-SNE visualizations and Wasserstein Distances (WD) across multimodal datasets

randomly shuffle to represent $\hat{z}^j$, thereby promoting sentiment classification in the **[L]** modality. For the **[V→A]** case with AVMNIST, we use randomly shuffled images from AVMNIST as $\hat{z}^j$ in audio classification tasks. For the **[A→V]** case in AVMNIST, $\hat{z}^j$ is generated by adding Gaussian noise to the audio data and apply shuffling, similar to the **[A→L]** case, to assist the classification task on PCA-projected MNIST images. Detail description of implementing $\hat{z}^j$ is provided on Table 5.

Implementation For the **[L→V]** case in ImageNet-1K classification task, we followed hyperparameter settings from the AugReg-ViT (Steiner et al., 2022) in training ResNet50, ViT-B/32, and ViT-B/16. For multimodal datasets, i.e., IEMOCAP and AVMNIST, particularly in the cases of **[L→A]**, **[A→L]**, **[V→A]** and **[A→V]**, we employed customized hyperparameter settings for each case. We consistently used 30 training epochs with Adam optimizer (Kingma & Ba, 2015). We omitted any data augmentations. Lastly, we applied $\alpha = 0.5$ for the **[L→V]** case, and $\alpha = 0.3$ for the other cases. Additional details, including learning rates, augmentations, schedulers and other relevant hyperparameters, are provided in Appendix B.

Details of the descriptions of the overall experiments are provided in Appendix B.

4.2 Results

Main Results Our main results are two parts: Table 1 with ImageNet-1K and Table 2 with multimodal datasets, i.e., IEMOCAP and AVMNIST.

According to Table 1, the results for the multimodal learning case, especially **[L→V]** case, highlights the outstanding performance of our approach on ImageNet-1K (IN). where it achieved improvements between $+1.5\%$ and $+2.5\%$. Notably, our approach also demonstrates significant improvements across additional evaluation datasets, including ImageNet-V2, out-of-distribution (OOD) datasets such as ImageNet-Rend. (Hendrycks et al., 2020), ImageNet-Sketch (Wang et al., 2019), and ImageNet-Style. (Geirhos et al., 2019), achieving performance gains between $+1.5\%$ and $+2.4\%$. Furthermore, our approach also excels in robustness benchmarks, achieving improvements of $+1.5\%$ to $+4.5\%$ on adversarial examples from ImageNet-A (Hendrycks et al., 2020) and corrupted images from ImageNet-C (Hendrycks & Dietterich, 2019). Surprisingly, language models clearly promote the training of visual models, i.e., writers indeed help painters. Noteworthy, the synergy shows consistent gains even in OOD, adversarial, and corrupted samples. It emphasizes that language models also facilitate visual models to acquire representations, which are well-generalized on a wide range of visual data distributions.

For more cases with IEMOCAP and AVMNIST in Table 2, our approach also leads to clear performance gains across various tests. In the IEMOCAP experiment, it shows a considerable gain of approximately $+1.6\%$ in the **[L→A]** case and $+0.6\%$ gain in the **[A→L]** case. For the AVMNIST testing, the performance improvement is around $+1.2\%$ in the **[A→L]** case and $+1.4\%$ in the **[A→L]** case. Importantly, we confirm that three modalities, i.e., V, L, and A, are shown to promote each other's training, which is not easily anticipated. It highlights the wide applicability of our claims in handling various kinds of modalities.

In addition, we emphasize that our claims are validated in many existing deep model architectures across modalities, which indicates the model-agnostic advantages of our claims.

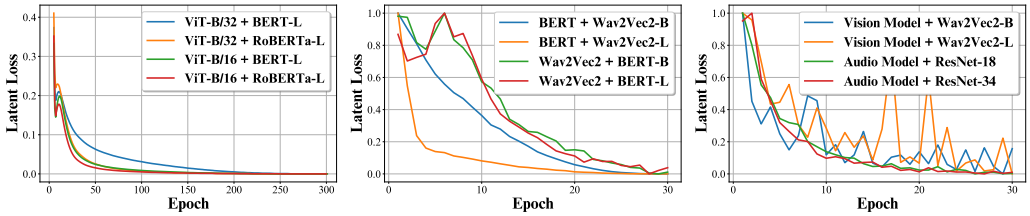

(a) ImageNet-1K $\mathcal{L}_z$ (b) IEMOCAP $\mathcal{L}_z$ (c) AVMNIST $\mathcal{L}_z$

Figure 4: Validation Latent loss $\mathcal{L}_z$ across the entire datasets

Table 3: Evaluation across the different value of α

Datasets	Accuracy				
	$\alpha = 0$	$\alpha = 0.1$	$\boldsymbol{\alpha = 0.3}$	$\alpha = 0.5$	$\alpha = 0.7$
IEMOCAP **[L→A]**	59.32	60.34	**61.20**	59.87	59.93
IEMOCAP **[A→L]**	55.20	55.51	**56.49**	54.19	55.90
AVMNIST **[V→A]**	41.28	42.03	**42.44**	41.77	41.79
AVMNIST **[A→V]**	64.79	65.03	**66.69**	64.77	64.76

Table 4: Comparison: $\hat{z}^j$ vs. z^j

Model [L→V]	$\hat{z}^j$	z^j
ResNet-50 + RoBERTa	76.90	76.95 (+0.05)
ViT-B/32 + RoBERTa	74.92	75.03 (+0.11)
ViT-B/16 + RoBERTa	79.58	79.81 (+0.22)

5 Analysis

5.1 Analysis and Representation Visualizations

Wasserstein Distance between Modalities Our hypothesis suggests that the Wasserstein distance between the latent feature distributions of individual modalities should exceed that of an adaptively trained distribution, $\hat{\mathcal{P}}_k$, which ideally lies between the latent spaces of the given modalities. Figure 3 illustrates this concept. In the test of $[M_j \rightarrow M_i]$ scenario, the denote latent vectors z^i from the M_i modality, represent $\{\hat{z}_m^k\}_{m=1}^M$, and represent M_j modality latent vectors z^j. As expected, t-SNE visualizations largely represent that $\hat{z}_m^k$ resides between the latent spaces of M_i and M_j, with asmaller Wasserstein distance to each modality (see $W_2(\cdot, \hat{\mathcal{P}}_k)$ terms), while individual modalities are shown to be distant to each other. These findings visually illustrate our hypothesis, coinciding with the claim of 'interpolated' representations. It further confirms that our $\mathcal{L}_{total}$ empirically serves as an adequate objective function to acquire the superior interpolate representation in between individual modalities.

The Convergence of Latent Loss We here show how the latent loss, i.e., $\mathcal{L}_z$, which reflects how much the interpolated representation moves close to the modality M_j, behaves during the training. As shown in Figure 4, the loss consistently decreases throughout all cases. This result highlights the narrowing gap between the latent vectors from modality M_j and the representation vectors derived from the input data. By minimizing this gap, the model successfully exploits simplified yet informative latent features $\hat{z}^j$, thereby improving overall performance. Since MSE loss is employed, the magnitude of the gap may vary across experiments due to the dimensions of representation vectors. To account for this, we applied normalized latent loss to observe a clear convergence. Despite some fluctuations of some cases, it is well-observed that losses consistently decrease and converge toward almost zero.

5.2 Ablation Studies

The Effect of $\boldsymbol{\alpha}$ Since α plays a crucial role in finding optimal latent space, we evaluated how variations in α influence performance on multimodal datasets. We tested various values of $\alpha = \{0.0, 0.1, 0.3, 0.5, 0.7\}$, and the corresponding results are shown in Table 3. We observe clear performance degradation when a biased α with too small or large values is used. It demonstrates that the biased cases, which tend to strongly rely on one single modality, do not show a synergy. Among candidates, $\alpha = 0.3$ consistently shows the best accuracies, highlighting the importance of balancing the contribution of each modality. When reminding t-SNE visualizations in Figure 3, α

with a moderate value coincides with the spatial position of the representation at the middle of two individual representations.

The Usage of Paired supervision $\mathcal{Z}^j$ vs. $\hat{\mathcal{Z}}^j$: Rather than using imperfect $\hat{z}^j$, we investigate how much gains would be further achieved when using the perfectly matched z^j. In Table 4, we tested the ImageNet-1K (IN) cases, where the column with '$\hat{z}^j$' refers to the numbers in Table 1 of the main experiments, and the column with 'z^j' is done with perfectly matched supervision in the **[L]** modality.[3] As shown in Table 4, although the performance slightly improves, the gains are minimal. This result aligns with our hypothesis, indicating that δ from Theorem 2 has a limited effect on performance, supporting our hypothesis. Also, the result emphasizes that our approach significantly relieves the cost of pairing perfectly matched supervision across modalities while achieving a comparative performance with the ideal case with paired supervision.

6 Further Discussions

Innovating Multimodal Learning: In prior works, many multimodal learning methods have relied on paired-datasets for training. This contrasts with human learning, which often occurs without the need for precisely paired object from different modality. Similar to human's perspective, our work seek to overcome this limitation, demonstrating that minimal or even imperfect supervision from different modalities can still enhance learning in the primary modality. Consequently, our approach suggest further advancements in technical perspective, enabling the effective utilization of multimodal settings even when only a single modality is available, as in the case of **[L→V]** with ImageNet-1K.

Discovery of unexpected synergy between modalities: It is commonly assumed that not every modality can effectively assist another. The prevailing notion is that unrelated modalities may not provide meaningful assistance to one another. However, our experiments on **[V→A]** and **[A→V]** reveal that cross-modality interactions, even between seemingly unrelated domains, can lead to significant performance improvements. These results demonstrate that integrating seemingly unrelated modalities can still yield benefits, uncovering hidden correlations and unexpected synergies between them. This approach opens new possibilities for exploring multimodal combinations that were previously considered non-beneficial, such as integrating language with signal-based sensory data. Expanding the scope of multimodal learning may reveal hidden synergies between multiple modalities, leading to improved overall performance.

Broad Impacts on Wide Range of Tasks: Recent works has focused on addressing the generalization problem, such as out-of-distribution (OOD), adverserial, and robustness. We validated that our method not only achieves strong performance on the ImageNet-1K but also shows significant improvements in OOD, adversarial, and robustness scenarios, as shown in Table 1. These findings suggest that our approach could be extended to further tackle the generalization problem by incorporating additional guidance from imperfect data across other modalities.

Limitations: Since our approach has been utilized only paired cases of modalities, it can be extended to incorporate more than two modalities in further approach. This could explore how multiple modalities might be leveraged to enhance the performance of a single modality. Moreover, the dimensionality of latent vector spaces often varies across modalities, requiring additional techniques to align these dimensions, which can impact overall performance.

7 Conclusions

We presented both theoretical and empirical evidence demonstrating that a modality with imperfect representation can still enhance learning in another modality. Our results and extensive analyses validate the proposed hypothesis and reinforce the theoretical foundations of this approach. Notably, we showed that paired supervision between datasets is unnecessary, as weakly related supervision or even mismatched setting across modalities can still lead to improvements. Finally, we propose future research to explore more complex multimodal settings, such as leveraging more than two modalities to assist another, which may drive significant advancements in this field.

[3] Additional details providing more precise information are included in the Appendix. B.

REFERENCES

Alexei Baevski, Yuhao Zhou, Abdelrahman Mohamed, and Michael Auli. wav2vec 2.0: A framework for self-supervised learning of speech representations. *Advances in neural information processing systems*, 33:12449–12460, 2020.

Peter L Bartlett and Shahar Mendelson. Rademacher and gaussian complexities: Risk bounds and structural results. *Journal of Machine Learning Research*, 3(Nov):463–482, 2002.

Tom Brown, Benjamin Mann, Nick Ryder, Melanie Subbiah, Jared D Kaplan, Prafulla Dhariwal, Arvind Neelakantan, Pranav Shyam, Girish Sastry, Amanda Askell, Sandhini Agarwal, Ariel Herbert-Voss, Gretchen Krueger, Tom Henighan, Rewon Child, Aditya Ramesh, Daniel Ziegler, Jeffrey Wu, Clemens Winter, Chris Hesse, Mark Chen, Eric Sigler, Mateusz Litwin, Scott Gray, Benjamin Chess, Jack Clark, Christopher Berner, Sam McCandlish, Alec Radford, Ilya Sutskever, and Dario Amodei. Language models are few-shot learners. In H. Larochelle, M. Ranzato, R. Hadsell, M.F. Balcan, and H. Lin (eds.), *Advances in Neural Information Processing Systems*, volume 33, pp. 1877–1901. Curran Associates, Inc., 2020. URL https://proceedings.neurips.cc/paper_files/paper/2020/file/1457c0d6bfcb4967418bfb8ac142f64a-Paper.pdf.

Carlos Busso, Murtaza Bulut, Chi-Chun Lee, Abe Kazemzadeh, Emily Mower, Samuel Kim, Jeannette N Chang, Sungbok Lee, and Shrikanth S Narayanan. Iemocap: Interactive emotional dyadic motion capture database. *Language resources and evaluation*, 42:335–359, 2008.

Ekin D Cubuk, Barret Zoph, Jonathon Shlens, and Quoc V Le. Randaugment: Practical automated data augmentation with a reduced search space. In *Proceedings of the IEEE/CVF conference on computer vision and pattern recognition workshops*, pp. 702–703, 2020.

Jacob Devlin, Ming-Wei Chang, Kenton Lee, and Kristina Toutanova. BERT: Pre-training of deep bidirectional transformers for language understanding. In Jill Burstein, Christy Doran, and Thamar Solorio (eds.), *Proceedings of the 2019 Conference of the North American Chapter of the Association for Computational Linguistics: Human Language Technologies, Volume 1 (Long and Short Papers)*, pp. 4171–4186, Minneapolis, Minnesota, June 2018. Association for Computational Linguistics. doi: 10.18653/v1/N19-1423. URL https://aclanthology.org/N19-1423.

Alexey Dosovitskiy, Lucas Beyer, Alexander Kolesnikov, Dirk Weissenborn, Xiaohua Zhai, Thomas Unterthiner, Mostafa Dehghani, Matthias Minderer, Georg Heigold, Sylvain Gelly, Jakob Uszkoreit, and Neil Houlsby. An image is worth 16x16 words: Transformers for image recognition at scale. *ICLR*, 2021.

Abhimanyu Dubey, Abhinav Jauhri, Abhinav Pandey, Abhishek Kadian, Ahmad Al-Dahle, Aiesha Letman, Akhil Mathur, Alan Schelten, Amy Yang, Angela Fan, et al. The llama 3 herd of models. *arXiv preprint arXiv:2407.21783*, 2024.

Robert Geirhos, Patricia Rubisch, Claudio Michaelis, Matthias Bethge, Felix A Wichmann, and Wieland Brendel. Imagenet-trained CNNs are biased towards texture; increasing shape bias improves accuracy and robustness. In *International Conference on Learning Representations*, 2019. URL https://openreview.net/forum?id=Bygh9j09KX.

Rohit Girdhar, Alaaeldin El-Nouby, Zhuang Liu, Mannat Singh, Kalyan Vasudev Alwala, Armand Joulin, and Ishan Misra. Imagebind: One embedding space to bind them all. In *Proceedings of the IEEE/CVF Conference on Computer Vision and Pattern Recognition*, pp. 15180–15190, 2023.

Kaiming He, Xiangyu Zhang, Shaoqing Ren, and Jian Sun. Deep residual learning for image recognition. In *Proceedings of the IEEE conference on computer vision and pattern recognition*, pp. 770–778, 2016.

Dan Hendrycks and Thomas Dietterich. Benchmarking neural network robustness to common corruptions and perturbations. *Proceedings of the International Conference on Learning Representations*, 2019.

Dan Hendrycks, Steven Basart, Norman Mu, Saurav Kadavath, Frank Wang, Evan Dorundo, Rahul Desai, Tyler Lixuan Zhu, Samyak Parajuli, Mike Guo, et al. The many faces of robustness: A critical analysis of out-of-distribution generalization. 2021 ieee. In *CVF International Conference on Computer Vision (ICCV)*, volume 2, 2020.

Yu Huang, Chenzhuang Du, Zihui Xue, Xuanyao Chen, Hang Zhao, and Longbo Huang. What makes multi-modal learning better than single (provably). *Advances in Neural Information Processing Systems*, 34:10944–10956, 2021.

Minyoung Huh, Brian Cheung, Tongzhou Wang, and Phillip Isola. Position: The platonic representation hypothesis. In *Forty-first International Conference on Machine Learning*, 2024. URL https://openreview.net/forum?id=BH8TYy0r6u.

Zohar Jackson, César Souza, Jason Flaks, Yuxin Pan, Hereman Nicolas, and Adhish Thite. Jakobovski/free-spoken-digit-dataset: v1. 0.8, 2018.

Donggeun Kim and Taesup Kim. Missing modality prediction for unpaired multimodal learning via joint embedding of unimodal models. In *European Conference on Computer Vision*, pp. 171–187. Springer, 2025.

Diederik P. Kingma and Jimmy Ba. Adam: A method for stochastic optimization. In Yoshua Bengio and Yann LeCun (eds.), *3rd International Conference on Learning Representations, ICLR 2015, San Diego, CA, USA, May 7-9, 2015, Conference Track Proceedings*, 2015. URL http://arxiv.org/abs/1412.6980.

Alex Krizhevsky, Geoffrey Hinton, et al. Learning multiple layers of features from tiny images. 2009.

Alex Krizhevsky, Ilya Sutskever, and Geoffrey E Hinton. Imagenet classification with deep convolutional neural networks. *Advances in Neural Information Processing Systems*, 25, 2012.

Tom Kwiatkowski, Jennimaria Palomaki, Olivia Redfield, Michael Collins, Ankur Parikh, Chris Alberti, Danielle Epstein, Illia Polosukhin, Jacob Devlin, Kenton Lee, et al. Natural questions: a benchmark for question answering research. *Transactions of the Association for Computational Linguistics*, 7:453–466, 2019.

Yann LeCun, Léon Bottou, Yoshua Bengio, and Patrick Haffner. Gradient-based learning applied to document recognition. *Proceedings of the IEEE*, 86(11):2278–2324, 1998.

Yi-Lun Lee, Yi-Hsuan Tsai, Wei-Chen Chiu, and Chen-Yu Lee. Multimodal prompting with missing modalities for visual recognition. In *Proceedings of the IEEE/CVF Conference on Computer Vision and Pattern Recognition*, pp. 14943–14952, 2023.

Hong Li, Xingyu Li, Pengbo Hu, Yinuo Lei, Chunxiao Li, and Yi Zhou. Boosting multi-modal model performance with adaptive gradient modulation. In *Proceedings of the IEEE/CVF International Conference on Computer Vision*, pp. 22214–22224, 2023.

Jian Li, Yong Liu, Rong Yin, Hua Zhang, Lizhong Ding, and Weiping Wang. Multi-class learning: From theory to algorithm. *Advances in Neural Information Processing Systems*, 31, 2018.

Junnan Li, Ramprasaath Selvaraju, Akhilesh Gotmare, Shafiq Joty, Caiming Xiong, and Steven Chu Hong Hoi. Align before fuse: Vision and language representation learning with momentum distillation. *Advances in neural information processing systems*, 34:9694–9705, 2021.

Paul Pu Liang, Yiwei Lyu, Xiang Fan, Zetian Wu, Yun Cheng, Jason Wu, Leslie Chen, Peter Wu, Michelle A Lee, Yuke Zhu, et al. Multibench: Multiscale benchmarks for multimodal representation learning. *Advances in neural information processing systems*, 2021(DB1):1, 2021.

Haotian Liu, Chunyuan Li, Qingyang Wu, and Yong Jae Lee. Visual instruction tuning. *Advances in neural information processing systems*, 36, 2024.

Yinhan Liu, Myle Ott, Naman Goyal, Jingfei Du, Mandar Joshi, Danqi Chen, Omer Levy, Mike Lewis, Luke Zettlemoyer, and Veselin Stoyanov. Roberta: A robustly optimized bert pretraining approach. *arXiv preprint arXiv:1907.11692*, 2019.

Ilya Loshchilov and Frank Hutter. SGDR: Stochastic gradient descent with warm restarts. In *International Conference on Learning Representations*, 2017. URL https://openreview.net/forum?id=Skq89Scxx.

Ilya Loshchilov and Frank Hutter. Decoupled weight decay regularization. In *International Conference on Learning Representations*, 2019. URL https://openreview.net/forum?id=Bkg6RiCqY7.

Guillaume Mahey, Laetitia Chapel, Gilles Gasso, Clément Bonet, and Nicolas Courty. Fast optimal transport through sliced generalized wasserstein geodesics. *Advances in Neural Information Processing Systems*, 36, 2024.

Paulius Micikevicius, Sharan Narang, Jonah Alben, Gregory Diamos, Erich Elsen, David Garcia, Boris Ginsburg, Michael Houston, Oleksii Kuchaiev, Ganesh Venkatesh, and Hao Wu. Mixed precision training. In *International Conference on Learning Representations*, 2018. URL https://openreview.net/forum?id=r1gs9JgRZ.

David Mizrahi, Roman Bachmann, Oguzhan Kar, Teresa Yeo, Mingfei Gao, Afshin Dehghan, and Amir Zamir. 4m: Massively multimodal masked modeling. *Advances in Neural Information Processing Systems*, 36, 2024.

Ziqi Pang, Ziyang Xie, Yunze Man, and Yu-Xiong Wang. Frozen transformers in language models are effective visual encoder layers. In *The Twelfth International Conference on Learning Representations*, 2024. URL https://openreview.net/forum?id=t0FI3Q66K5.

Adam Paszke, Sam Gross, Francisco Massa, Adam Lerer, James Bradbury, Gregory Chanan, Trevor Killeen, Zeming Lin, Natalia Gimelshein, Luca Antiga, et al. Pytorch: An imperative style, high-performance deep learning library. *Advances in neural information processing systems*, 32, 2019.

Juan-Manuel Pérez-Rúa, Valentin Vielzeuf, Stéphane Pateux, Moez Baccouche, and Frédéric Jurie. Mfas: Multimodal fusion architecture search. In *Proceedings of the IEEE/CVF Conference on Computer Vision and Pattern Recognition*, pp. 6966–6975, 2019.

Gabriel Peyré and Marco Cuturi. Computational optimal transport. *Foundations and Trends in Machine Learning*, 11(5-6):355–607, 2019.

Alec Radford, Jong Wook Kim, Chris Hallacy, Aditya Ramesh, Gabriel Goh, Sandhini Agarwal, Girish Sastry, Amanda Askell, Pamela Mishkin, Jack Clark, et al. Learning transferable visual models from natural language supervision. In *International Conference on Machine Learning*, pp. 8748–8763. PMLR, 2021.

Mirco Ravanelli, Titouan Parcollet, Peter Plantinga, Aku Rouhe, Samuele Cornell, Loren Lugosch, Cem Subakan, Nauman Dawalatabad, Abdelwahab Heba, Jianyuan Zhong, Ju-Chieh Chou, Sung-Lin Yeh, Szu-Wei Fu, Chien-Feng Liao, Elena Rastorgueva, François Grondin, William Aris, Hwidong Na, Yan Gao, Renato De Mori, and Yoshua Bengio. SpeechBrain: A general-purpose speech toolkit, 2021. arXiv:2106.04624.

Benjamin Recht, Rebecca Roelofs, Ludwig Schmidt, and Vaishaal Shankar. Do imagenet classifiers generalize to imagenet? In *International conference on machine learning*, pp. 5389–5400. PMLR, 2019.

Joshua David Robinson, Ching-Yao Chuang, Suvrit Sra, and Stefanie Jegelka. Contrastive learning with hard negative samples. In *International Conference on Learning Representations*, 2021. URL https://openreview.net/forum?id=CR1XOQ0UTh-.

Pratyusha Sharma, Tamar Rott Shaham, Manel Baradad, Stephanie Fu, Adrian Rodriguez-Munoz, Shivam Duggal, Phillip Isola, and Antonio Torralba. A vision check-up for language models. In *Proceedings of the IEEE/CVF Conference on Computer Vision and Pattern Recognition*, pp. 14410–14419, 2024.

Andreas Peter Steiner, Alexander Kolesnikov, Xiaohua Zhai, Ross Wightman, Jakob Uszkoreit, and Lucas Beyer. How to train your vit? data, augmentation, and regularization in vision transformers. *Transactions on Machine Learning Research*, 2022. ISSN 2835-8856. URL https://openreview.net/forum?id=4nPswr1KcP.

Alon Talmor, Jonathan Herzig, Nicholas Lourie, and Jonathan Berant. Commonsenseqa: A question answering challenge targeting commonsense knowledge. *arXiv preprint arXiv:1811.00937*, 2018.

Hugo Touvron, Thibaut Lavril, Gautier Izacard, Xavier Martinet, Marie-Anne Lachaux, Timothée Lacroix, Baptiste Rozière, Naman Goyal, Eric Hambro, Faisal Azhar, et al. Llama: Open and efficient foundation language models. *arXiv preprint arXiv:2302.13971*, 2023a.

Hugo Touvron, Louis Martin, Kevin Stone, Peter Albert, Amjad Almahairi, Yasmine Babaei, Nikolay Bashlykov, Soumya Batra, Prajjwal Bhargava, Shruti Bhosale, et al. Llama 2: Open foundation and fine-tuned chat models. *arXiv preprint arXiv:2307.09288*, 2023b.

Samarth Tripathi, Sarthak Tripathi, and Homayoon Beigi. Multi-modal emotion recognition on iemocap dataset using deep learning. *arXiv preprint arXiv:1804.05788*, 2018.

Yao-Hung Hubert Tsai, Paul Pu Liang, Amir Zadeh, Louis-Philippe Morency, and Ruslan Salakhutdinov. Learning factorized multimodal representations. In *International Conference on Learning Representations*, 2019. URL https://openreview.net/forum?id=rygqqsA9KX.

Ashish Vaswani, Noam Shazeer, Niki Parmar, Jakob Uszkoreit, Llion Jones, Aidan N Gomez, Ł ukasz Kaiser, and Illia Polosukhin. Attention is all you need. In I. Guyon, U. Von Luxburg, S. Bengio, H. Wallach, R. Fergus, S. Vishwanathan, and R. Garnett (eds.), *Advances in Neural Information Processing Systems*, volume 30. Curran Associates, Inc., 2017.

Valentin Vielzeuf, Alexis Lechervy, Stéphane Pateux, and Frédéric Jurie. Centralnet: a multilayer approach for multimodal fusion. In *Proceedings of the European Conference on Computer Vision (ECCV) Workshops*, pp. 0–0, 2018.

Cédric Villani et al. *Optimal transport: old and new*, volume 338. Springer, 2009.

Haohan Wang, Songwei Ge, Zachary Lipton, and Eric P Xing. Learning robust global representations by penalizing local predictive power. In *Advances in Neural Information Processing Systems*, pp. 10506–10518, 2019.

Jianwei Yang, Chunyuan Li, Pengchuan Zhang, Bin Xiao, Ce Liu, Lu Yuan, and Jianfeng Gao. Unified contrastive learning in image-text-label space. In *Proceedings of the IEEE/CVF Conference on Computer Vision and Pattern Recognition*, pp. 19163–19173, 2022.

Amir Zadeh, Minghai Chen, Soujanya Poria, Erik Cambria, and Louis-Philippe Morency. Tensor fusion network for multimodal sentiment analysis. In Martha Palmer, Rebecca Hwa, and Sebastian Riedel (eds.), *Proceedings of the 2017 Conference on Empirical Methods in Natural Language Processing*, pp. 1103–1114, Copenhagen, Denmark, September 2017. Association for Computational Linguistics. doi: 10.18653/v1/D17-1115. URL https://aclanthology.org/D17-1115.

Hongyi Zhang, Moustapha Cisse, Yann N. Dauphin, and David Lopez-Paz. mixup: Beyond empirical risk minimization. In *International Conference on Learning Representations*, 2018. URL https://openreview.net/forum?id=r1Ddp1-Rb.

Andy Zhou, Jindong Wang, Yu-Xiong Wang, and Haohan Wang. Distilling out-of-distribution robustness from vision-language foundation models. In *Thirty-seventh Conference on Neural Information Processing Systems*, 2023. URL https://openreview.net/forum?id=iwp3H8uSeK.

Kaiyang Zhou, Jingkang Yang, Chen Change Loy, and Ziwei Liu. Conditional prompt learning for vision-language models. In *Proceedings of the IEEE/CVF conference on computer vision and pattern recognition*, pp. 16816–16825, 2022a.

Kaiyang Zhou, Jingkang Yang, Chen Change Loy, and Ziwei Liu. Learning to prompt for vision-language models. *International Journal of Computer Vision*, 130(9):2337–2348, 2022b.

A Mathematical Details for Theoratical Perspectives

A.1 Notations

We recall overall notations that has been used in this paper:

Notations	Descriptions
$\mathcal{X}, \mathcal{Z}, \mathcal{Y}$	Each is referred to as the input space, latent space, and hypothesis space.
$\mathcal{S}^i = \{(\mathbf{x}^i_m, y^i_m)\}^M_{m=1}$	The M_i dataset consists of M sampled datapoints, serving as the primary dataset for training.
$\mathcal{S}^j = \{\hat{\mathbf{x}}^j_m\}^M_{m=1}$	The M_j dataset consists of M sampled datapoints, serving as the synergy for training by providing restricted knowledge.
$g_i(\cdot), g_j(\cdot)$	Latent Space Mapping Function on each modality M_i and M_j $g_i(\cdot) : \mathcal{X}^i \to \mathcal{Z}^i$ and $g_j(\cdot) : \mathcal{X}^j \to \hat{\mathcal{Z}}^j$
$z^i, z^j, \hat{z}^j, z^\star$	Each is referred to as the latent feature derived from the function g applied to the input datasets for each modality.
$\mathcal{Z}^i, \mathcal{Z}^j, \hat{\mathcal{Z}}^j, \mathcal{Z}^\star$	Each is referred to as the latent space that contains all possible latent vectors correspoinding to each modality.
$h(\cdot)$	Hypothesis Space Mapping Function $\Rightarrow h(\cdot) : \mathcal{Z} \to \mathcal{Y}$
$\mathcal{P}_i, \mathcal{P}_j, \hat{\mathcal{P}}_j, \mathcal{P}_\star$	Each is referred to as the empirical distribution of modality's latent vectors and true latent vectors within the corresponding constructed spaces.

These notations are introduced in the **Definition**s and **Assumption**s outlined in Section 3.

A.2 Proof of Theorem 1 and Corollary 1.1

Theorem 1. *The optimal α^* that minimizes Δ_k is formulated as follows:*

$$\alpha^* = \frac{\Delta_i^2 - \Delta_j^2 + \Delta_{ij}^2}{2\Delta_{ij}^2}$$

Moreover, the resulting interpolated representation satisfies $\Delta_k \leq \Delta_i$ and $\Delta_k \leq \Delta_j$.

Proof. Since Wasserstein distance is symmetric and satisfies triangle inequality (Villani et al., 2009; Peyré & Cuturi, 2019), we can define the relationship each distribution of latent spaces:

$$W_2(\mathcal{P}_i, \mathcal{P}_j) \leq W_2(\mathcal{P}_\star, \mathcal{P}_i) + W_2(\mathcal{P}_\star, \mathcal{P}_j) \tag{10}$$

and this could be simplified via notations provided on Section A.1:

$$\Delta_{ij} \leq \Delta_i + \Delta_j \tag{11}$$

According to prior works (Villani et al., 2009; Peyré & Cuturi, 2019; Mahey et al., 2024), we can define a new equation as follows:

Definition 5 (**Generalized Geodesics** (Mahey et al., 2024))**.** *According to the convexity property of 2-Wasserstein distance, squared 2-Wasserstein distance betwen $\mathcal{P}_k$ and $\mathcal{P}_\star$ is bounded by:*

$$W_2^2(\mathcal{P}_k, \mathcal{P}_\star) \leq (1-\alpha)W_2^2(\mathcal{P}_\star, \mathcal{P}_i) + \alpha W_2^2(\mathcal{P}_\star, \mathcal{P}_j) - \alpha(1-\alpha)W_2^2(\mathcal{P}_i, \mathcal{P}_j) \tag{12}$$

$$= (1-\alpha)\Delta_i^2 + \alpha\Delta_j^2 - \alpha(1-\alpha)\Delta_{ij}^2 \tag{13}$$

Since our primary goal is to determine the optimal α, we can express Equation 13 as the quadratic function of α, i.e., $f(\alpha) = (1-\alpha)\Delta_i^2 + \alpha\Delta_j^2 - \alpha(1-\alpha)\Delta_{ij}^2$. The optimal value of α can then be determined by taking the derivative of the function $f(\alpha)$:

$$\frac{\partial f(\alpha)}{\partial \alpha} = -\Delta_i^2 + \Delta_j^2 - (1-2\alpha)\Delta_{ij}^2 = 0 \tag{14}$$

Changing into the term of α is then :

$$\alpha^* = \frac{1}{2}\left(1 + \frac{\Delta_i^2 - \Delta_j^2}{\Delta_{ij}^2}\right) = \frac{1+C}{2} \quad \text{where } C = \frac{(\Delta_i + \Delta_j)(\Delta_i - \Delta_j)}{\Delta_{ij}^2} \tag{15}$$

where $\alpha^* = \arg\min_{\alpha} f(\alpha)$. This optimal α^* remains valid under the Assumption 1 that Δ_{ij} is bigger than 0, ensuring that α^* does not diverge.

It still remains to be proven that the optimal value of α^* indeed minimizes Δ_k and satisfies the condition that Δ_k is smaller than both Δ_i and Δ_j. To establish this, we begin by verifying if Δ_k is truly minimized. Let the minimized value of Δ_k be denoted as Δ_k^*. Assume that $z^k \sim \mathcal{P}_k$ lies on the geodesic between $z^i \sim \mathcal{P}_i$ and $z^j \sim \mathcal{P}_j$, representing a projection onto the true latent space.[4]

To demonstrate this, we can apply the Pythagorean theorem. Under the above assumption, Δ_k^* can be expressed as:

$$\begin{aligned} {\Delta_k^*}^2 &= \Delta_i^2 - (\alpha\Delta_{ij})^2 && (16)\\ &= \Delta_j^2 - ((1-\alpha)\Delta_{ij})^2 && (17) \end{aligned}$$

We can further rearrange the above equations as:

$$\Delta_i^2 - \Delta_j^2 = (2\alpha - 1)\Delta_{ij}^2 \tag{18}$$

From this, we solve for optimal α, denoted as α^*:

$$\alpha^* = \frac{1}{2}\left(1 + \frac{\Delta_i^2 - \Delta_j^2}{\Delta_{ij}^2}\right) \tag{19}$$

This expression corresponds to the optimal value α^* from Equation 4 and satisfies the Pythagorean theorem, which we assumed to hold when minimizing Δ_k. This minimized value of Δ_k represents the distance between $\mathcal{P}_\star$ and the distribution $\mathcal{P}_k$, projected directly onto the geodesic connecting $\mathcal{P}_i$ and $\mathcal{P}_j$. Moreover, we conclude that the minimized Δ_k^* is indeed smaller than both Δ_i and Δ_j, where ${\Delta_k^*}^2 \leq \Delta_i^2$ as related to Equation 16 and ${\Delta_k^*}^2 \leq \Delta_j^2$ as related to Equation 17. Therefore, result is formally expressed as:

$$\Delta_k^* \leq \min(\Delta_i, \Delta_j) \tag{20}$$

where it satisfies the Theorem 1.□

Corollary 1.1 *The optimal α^* is bounded as follows:*

$$\alpha^* = \begin{cases} \left[\dfrac{\Delta_i}{\Delta_i + \Delta_j}, 1\right] & \textit{if } \Delta_i > \Delta_j \\[2ex] \left[0, \dfrac{\Delta_i}{\Delta_i + \Delta_j}\right] & \textit{otherwise} \end{cases}$$

Proof. To establish the validity of the optimal α^* under different conditions for Δ_i and Δ_j, we begin by examining the relationship between these two quantities.

- **Condition 1.1: $(\boldsymbol{\Delta_i > \Delta_j})$** : This scenario implies that the difference between Δ_i and Δ_j is positive, meaning $C = \frac{\Delta_i - \Delta_j}{\Delta_i + \Delta_j}$ exhibits a positive value. In this case, the constant C is bounded by the inequality:

$$C \geq \frac{\Delta_i - \Delta_j}{\Delta_i + \Delta_j} \tag{21}$$

[4]This concept is detailed in the min-SWDD paper (Mahey et al., 2024).

Substituting this bound into Equation 15, we have the following inequality for the optimal value of α^*:

$$\alpha^* \geq \frac{1}{2}\left(1 + \frac{\Delta_i - \Delta_j}{\Delta_i + \Delta_j}\right) \tag{22}$$

$$= \frac{\Delta_i}{\Delta_i + \Delta_j} \tag{23}$$

Since we know that α^* is constrained by $0 \leq \alpha^* \leq 1$, this inequality confirms that $\alpha^* = \frac{\Delta_i}{\Delta_i + \Delta_j}$ satisfies the first condition of optimality, as given by Equation 5. This ensures that when $\Delta_i > \Delta_j$, the chosen value of α^* lies within the allowable range and maintains the necessary relationship between the distances.

- **Condition 1.2:** $(\boldsymbol{\Delta_i \leq \Delta_j})$: In this case, the difference between Δ_i and Δ_j is non-positive, and consequently, the value of C becomes negative. Thus, the constant C is bounded by the inequality:

$$C \leq \frac{\Delta_i - \Delta_j}{\Delta_i + \Delta_j} \tag{24}$$

By applying the same process as in Condition 1, we substitute this bound into the formula for α^*, yielding:

$$\alpha^* \leq \frac{\Delta_i}{\Delta_i + \Delta_j} \tag{25}$$

Since α^* must satisfy $0 \leq \alpha^* \leq 1$, this condition is similarly met. Given that $\alpha^* \geq 0$, this value conforms to the second condition of optimality in Equation 5. Hence, when $\Delta_i \leq \Delta_j$, the optimal value of α^* continues to fulfill the constraints of the inequality, ensuring that the geometric relationship between the distances is preserved.

Thus, the optimal value α^* satisfies both conditions for the two possible relationships between Δ_i and Δ_j, concluding the proof. □

A.3 Proof of Theorem 2 and Corollary 2.1

Theorem 2. *Let $\hat{z}^k \in \hat{\mathcal{Z}}^k$ be the interpolated latent space between the M_i and the restricted M_j, defined by the interpolation coefficient α as: $\hat{\mathcal{Z}}^k = \{\hat{z}^k = (1-\alpha)z^i + \alpha\hat{z}^j \mid z^i \in \mathcal{Z}^i, \hat{z}^j \in \hat{\mathcal{Z}}^j\}$, where $\hat{\mathcal{P}}_k$ represents its distribution. Let the 2-Wasserstein distance between $\hat{\mathcal{P}}_k$ and $\mathcal{P}_\star$ be denoted as $W_2(\mathcal{P}_\star, \hat{\mathcal{P}}_k) = \hat{\Delta}_k$. Then the optimal $\hat{\alpha}^*$ that minimizes $\hat{\Delta}_k$ is formulated as follows: $\hat{\Delta}_k$:*

$$\hat{\alpha}^* = \frac{\Delta_i^2 - \hat{\Delta}_j^2 + \hat{\Delta}_{ij}^2}{2\hat{\Delta}_{ij}^2}$$

Moreover, the resulting interpolated representation satisfies $\hat{\Delta}_k \leq \Delta_i$ and $\hat{\Delta}_k \leq \hat{\Delta}_j$.

Proof. Similar to the approach in Appendix A.2, $\hat{\Delta}_k$ can be defined with following Definition 5:

$$W_2^2(\mathcal{P}_\star, \hat{\mathcal{P}}_k) \leq (1-\alpha)W_2^2(\mathcal{P}_\star, \mathcal{P}_i) + \alpha W_2^2(\mathcal{P}_\star, \hat{\mathcal{P}}_j) - \alpha(1-\alpha)W_2^2(\mathcal{P}_i, \hat{\mathcal{P}}_j) \tag{26}$$

$$= (1-\alpha)\Delta_i^2 + \alpha\hat{\Delta}_j^2 - \alpha(1-\alpha)\hat{\Delta}_{ij}^2 \tag{27}$$

To determine the optimal α that minimizes the left-hand side of Equation 27, we can utilize the derivative of the function $f(\alpha) = (1-\alpha)\Delta_i^2 + \alpha\hat{\Delta}_j^2 - \alpha(1-\alpha)\hat{\Delta}_{ij}^2$ and set it equal to zero, as demonstrated in Equation 14:

$$\frac{\partial f(\alpha)}{\partial \alpha} = -\Delta_i^2 + \hat{\Delta}_j^2 - (1-2\alpha)\hat{\Delta}_{ij}^2 = 0. \tag{28}$$

This can be rephrased in terms of α, analogous to Equation 15:

$$\hat{\alpha}^* = \frac{1}{2}\left(1 + \frac{\Delta_i^2 - \hat{\Delta}_j^2}{\hat{\Delta}_{ij}^2}\right) = \frac{1 + C'}{2}, \quad \text{where } C' = \frac{(\Delta_i + \hat{\Delta}_j)(\Delta_i - \hat{\Delta}_j)}{\hat{\Delta}_{ij}^2} \tag{29}$$

Additionally, the optimal $\hat{\alpha}^*$ is valid, similar to the validity of α^*, under Assumption 1 and the property of $\hat{\Delta}_{ij}$, where $\Delta_{ij} \leq \hat{\Delta}_{ij}$.

To achieve the goal of minimizing $\hat{\Delta}_k$, we need to demonstrate that applying the optimal $\hat{\alpha}^*$ results in a value of $\hat{\Delta}_k$ smaller than both Δ_i and $\hat{\Delta}_j$. Following the previous steps outlined in the proof of Theorem 1, we can proceed as follows.

Let the minimized distance be denoted as $\hat{\Delta}_k^*$, with the optimal coefficient being $\hat{\alpha}^*$. Using the Pythagorean Theorem, we relate the distances Δ_i, $\hat{\Delta}_j$, and $\hat{\Delta}_{ij}$ through the following expressions:

$$\hat{\Delta}_k^{*2} = \Delta_i^2 - (\hat{\alpha}^* \hat{\Delta}_{ij})^2 \tag{30}$$

$$= \hat{\Delta}_j^2 - ((1 - \hat{\alpha}^*)\hat{\Delta}_{ij})^2 \tag{31}$$

These two equations can be rearranged in terms of $\hat{\alpha}^*$, leading to the expression:

$$\Delta_i^2 - \hat{\Delta}_j^2 = (2\hat{\alpha}^* - 1)\hat{\Delta}_{ij}^2 \tag{32}$$

From this, solving for $\hat{\alpha}^*$ yields:

$$\hat{\alpha}^* = \frac{1}{2}\left(1 + \frac{\Delta_i^2 - \hat{\Delta}_j^2}{\hat{\Delta}_{ij}^2}\right) \tag{33}$$

This expression is equivalent to Equation 8 in Theorem 2. The assumption that the optimal $\hat{\alpha}^*$ minimizes $\hat{\Delta}_k^*$, which denotes the geodesic projection of the distribution $\hat{\mathcal{P}}_k$ between $\mathcal{P}_i$ and $\hat{\mathcal{P}}_j$, aligns with the closed-form solution for $\hat{\alpha}^*$ given in Definition 5 and Equation 29.

Furthermore, by substituting into Equations 30 and 31, the minimization of $\hat{\Delta}_k^2$ implies:

$$\hat{\Delta}_k^2 \leq \min(\Delta_i^2, \hat{\Delta}_j^2) \tag{34}$$

$$\Rightarrow \hat{\Delta}_k \leq \min(\Delta_i, \hat{\Delta}_j) \tag{35}$$

Based on Definition 4 and the triangle inequality, $\hat{\Delta}_j$ can be further bounded as $\hat{\Delta}_j \leq \Delta_j + \delta$. However, as discussed in Remark 2.1, the term δ is expected to have a negligible effect on the Wasserstein distance between the distributions, resulting in only a minor constant offset. Therefore, this does not significantly impact the Wasserstein distance between the distributions, which Equation 35 will approximately similar to Equation 20. □

Corollary 2.1 *The optimal $\hat{\alpha}^*$ is bounded as follows:*

$$\hat{\alpha}^* = \begin{cases} \left[\dfrac{\Delta_i}{\Delta_i + \Delta_j + \delta}, 1\right] & \textit{if } \Delta_i > \hat{\Delta}_j \\ \left[0, \dfrac{\Delta_i}{\Delta_i + \Delta_j}\right] & \textit{otherwise} \end{cases}$$

Proof. We analyze the bounds on $\hat{\alpha}^*$ by considering two conditions based on Δ_i and $\hat{\Delta}_j$:

- **Condition 2.1 ($\boldsymbol{\Delta_i > \hat{\Delta}_j}$)**: In this case, C' is positive. From the triangle inequality for the 2-Wasserstein distance, we obtain the following lower bound:

$$C' \geq \frac{\Delta_i - \hat{\Delta}_j}{\Delta_i + \hat{\Delta}_j} \tag{36}$$

  Substituting this bound into Equation 29, we derive:

$$\hat{\alpha}^* \geq \frac{\Delta_i}{\Delta_i + \hat{\Delta}_j} \tag{37}$$

$$\geq \frac{\Delta_i}{\Delta_i + \Delta_j + \delta} \tag{38}$$

  where δ is a small constant, accounting for minor deviations between $\hat{\Delta}_j$ and Δ_j, as discussed in Remark 2.1. Since $\hat{\alpha}^* \leq 1$, this satisfies the first condition in Equation 9.

- **Condition 2.2 ($\boldsymbol{\Delta_i \leq \hat{\Delta}_j}$)**: In this scenario, C' becomes negative. Using a similar approach as in Case 1, the upper bound for C' is:

$$C' \leq \frac{\Delta_i - \hat{\Delta}_j}{\Delta_i + \hat{\Delta}_j} \tag{39}$$

Substituting this into Equation 29, we get:

$$\hat{\alpha}^* \leq \frac{\Delta_i}{\Delta_i + \hat{\Delta}_j} \tag{40}$$

Since $\hat{\Delta}_j \geq \Delta_j$, we can substitute $\hat{\Delta}_j$ with Δ_j, resulting in a looser bound:

$$\hat{\alpha}^* \leq \frac{\Delta_i}{\Delta_i + \Delta_j} \tag{41}$$

Thus, this bound satisfies the second condition of Equation 9.

Therefore, we find that the derived bounds on $\hat{\alpha}^*$ fulfill the both conditions stated in Equation 9. □

B Implementation Details

B.1 Datasets

ImageNet-1K and Evaluation Benchmarks ImageNet-1K (Krizhevsky et al., 2012) is the image datasets that contains 1000 classes with 1,281,167 training images and 50,000 validation images. ImageNet has been widely used in image classification benchmarks in various methoods, especially in computer vision task (Dosovitskiy et al., 2021; Steiner et al., 2022; Zhou et al., 2023; Pang et al., 2024). In our evaluation, we also assessed ImageNet-related validation benchmarks focusing on out-of-distribution (OOD) and robustness scenarios. These benchmarks can be categorized into three types: in-domain, OOD, and robustness.

For the in-domain category, we utilized ImageNet-V2 (Recht et al., 2019), which consists of 10 images per class from the original ImageNet-1K, with total 10,000 images. The OOD benchmarks contains ImageNet-Rendition (Hendrycks et al., 2020), ImageNet-Sketch (Wang et al., 2019), and ImageNet-Stylized (Geirhos et al., 2019). ImageNet-Rendition features 200 classes with a total of 30,000 images, while ImageNet-Sketch contains approximately 50 images per class, totaling 50,889 images sourced from Google image queries labeled as "`sketch of {class name}`." Lastly, the robustness scenarios encompass ImageNet-A (Hendrycks et al., 2020) and ImageNet-C (Hendrycks & Dietterich, 2019). ImageNet-A consists of images misclassified by the ResNet-50 model. ImageNet-C features a variety of generated corruptions, such as Gaussian noise and blurring, and is commonly used in adversarial training approaches.

IEMOCAP The IEMOCAP dataset (Busso et al., 2008) contains video, language and audio modalities. It consists of 151 recorded dialogue videos featuring two speakers per session, resulting in a total of 302 videos. Each segment is annotated for nine emotions: angry, excited, fear, sad, surprised, frustrated, happy, disappointed, and neutral. Recorded across five sessions with five pairs of speakers. It also contains the audio and script for each video data. IEMOCAP dataset is a valuable resource for research in multimodal emotion recognition and has been widely employed in various multimodal methods (Tripathi et al., 2018; Li et al., 2018) for the emotion sentiment classification.

As mentioned in Section 4.1, our implementation focused solely on the script and audio components, emphasizing the language and audio modalities. For convenience, we narrowed our analysis to six specific emotions: neutral, happy, angry, sad, excited, and frustrated, employing the official PyTorch framework (Paszke et al., 2019) for dataloader.

AVMNIST The AVMNIST dataset (Vielzeuf et al., 2018) contains digit images (0 to 9) from the MNIST dataset (LeCun et al., 1998), where each image has dimensions of $28 \times 28 \times 1$. These images have been subjected to PCA projection, resulting in a reduced information representation compared to the original MNIST dataset. In addition to the visual modality, the dataset includes an

audio modality from the Free Spoken Digits Dataset (FSDD) (Jackson et al., 2018). The audio data has been preprocessed into mel-frequency spectrograms, sampled at a resolution of $112 \times 112 \times 1$.

In the context of the audio modality [A], we approach the two cases, **[V→A]** and **[A→V]**, using distinct strategies. For the **[V→A]** case, the audio modality is processed using convolutional neural networks (CNNs), outlined in AGM (Li et al., 2023). In contrast, for the **[A→V]** case, we utilize raw audio data from the FSDD dataset rather than mel-spectrogram images, as pretrained models specifically trained on spectrogram data are not readily available for this task.

Representation of z^j In Section 5.2, we discussed the representation of z^j. Since ImageNet-1K does not contains any supervision related to the **[L]** modality, except class label, we employed a new description for each image generated by LLaVA (Liu et al., 2024). Specifically, we input images from ImageNet along with the following prompt: `"USER: <image>\nWhat does this image represent? Explain in a sentence.\nASSISTANT:"`. LLaVA generates a descriptive prompt for each image, which provides a description that is closer to the true supervision of the language modality, z^j, compared to our original prompt, `"This is a class about #."`, $\hat{z}^j$. As demonstrated in Table 4, this change does not result in significant performance differences, where it aligns to our theoretical perspective in Theorem 2 and Remark 2.1 that δ does not substantially affect the distance between the distributions of each modality.

B.2 Additional Experimental Settings

Pseudo code and detail implementation of $\hat{z}^j$ We provide the pseudo-code on Algorithm 1 and implementation details for $\hat{z}^j_m$ in all cases in Table 5 as follows:

Algorithm 1 Traininig Procedures for $[M_j \rightarrow M_i]$

Hyperparameter: α: interpolate coefficients, $\mathcal{B}$: batch size
Input: $\{(x^i_m, y^i_m)\}^M_{m=1} \sim \mathcal{S}^i$: input data from M_i modality sampled in batch size $\mathcal{B}$ for each, $\{\hat{x}^j_m\}^M_{m=1} \sim \mathcal{S}^j$: imperfect input data from M_j modality sampled in batch size $\mathcal{B}$ for each
Required: $\mathcal{L}_{CE}$: Cross-Entropy Loss, θ_i: M_i modality model parameters
Function: $g_i(\cdot;\theta_i)$: latent feature mapping function of M_i modality, $g_j(\cdot;\theta_j)$: latent feature mapping function of M_j modality, $h_i(\cdot;\theta_i)$: hypothesis function of M_i modality

while not done **do**
  for $m = 1, \ldots, M$ **do**
    $z^k_m = g_i(x^i_m;\theta_i)$
    $\hat{z}^j_m = g_j(\hat{x}^j_m;\theta_j)$
    $\mathcal{L}_{cls} = \mathcal{L}_{CE}(h_i(z^k_m;\theta_i), y^i_m)$
    $\mathcal{L}_z = \mathbb{E}\left[\frac{1}{2}||z^k_m - \hat{z}^j_m||^2_2\right]$
    $\mathcal{L}_{total} = (1-\alpha)\mathcal{L}_{cls} + \alpha\mathcal{L}_z$
    $\theta_i \leftarrow \theta_i - \nabla_{\theta_i}\mathcal{L}_{total}$
  end for
end while

Table 5: Implementation details of $\hat{z}^j_m$ across different datasets and cases

Datasets & Cases	Implementation of $\hat{z}^j_m$
ImageNet-1k [**L**→**V**]	**[L]** ⇒ `This is about Class #.`†
IEMOCAP [**L**→**A**]	**[L]** ⇒ `This is about Emotion #.`†
IEMOCAP [**A**→**L**]	**[A]** ⇒ Add Gaussian Noise: $\xi \sim \mathcal{N}(0, \lambda I)$†† & Random Shuffling
AVMNIST [**V**→**A**]	**[V]** ⇒ Random Shuffled Image (mismatch paired sets)
AVMNIST [**A**→V]	**[A]** ⇒ Add Gaussian Noise: $\xi \sim \mathcal{N}(0, \lambda I)$†† & Random Shuffling

†: # is a random number that does not directly correspond to the actual label.
††: λ is a parameter that controls the variance of the Gaussian noise. We applied $\lambda = 10^{-3}$

Hyperparameters Settings In the **[L→V]** case for the ImageNet-1K classification task, we adhered to the hyperparameter settings established by AugReg-ViT (Steiner et al., 2022) for all training models, specifically ResNet-50, ViT-B/32, and ViT-B/16. For the baseline model, we trained for 300 epochs with a batch size of 2048, utilizing a learning rate of 1×10^{-3} and a weight decay of 5×10^{-4}. We employed the AdamW optimizer (Loshchilov & Hutter, 2019) with cosine learning rate scheduling (Loshchilov & Hutter, 2017) and implemented a linear warmup for 20 epochs. Data augmentations, including MixUp (Zhang et al., 2018), RandAugment (Cubuk et al., 2020), and AugReg (Steiner et al., 2022), were applied throughout the training process. Furthermore, we utilized Automatic Mixed Precision (Micikevicius et al., 2018) in conjunction with four A6000 GPUs.

For the multimodal datasets, we customized two hyperparameter settings configuration based on the datasets: IEMOCAP dataset for fine-tuning and AVMNIST dataset for training from scratch. In the fine-tuning approach, particularly for the cases of **[L→A]** and **[A→L]**, we conducted training for 30 epochs with a batch size of 4. Given that the learning procedure is fine-tuning, we adjusted the learning rate to 5×10^{-5} and the weight decay to 5×10^{-4}, while also applying cosine learning rate scheduling (Loshchilov & Hutter, 2017). The Adam optimizer (Kingma & Ba, 2015) was employed, and no data augmentations were utilized. For training from scratch, specifically in the cases of **[L→V]** and **[A→V]** on the AVMNIST dataset, we again trained for 30 epochs with a batch size of 32. The learning rate was set to 1×10^{-3}, with a reduction factor of 0.1 applied at 25 epochs. The Adam optimizer (Kingma & Ba, 2015) was used, and data augmentations were omitted during this training phase as well.

Revisiting the value of α, we set $\alpha = 0.5$ for the case of **[L→V]** on ImageNet-1K dataset, and $\alpha = 0.3$ was employed for all other cases on IEMOCAP and AVMNIST dataset.

C Additional Ablation Study

C.1 Design choices in Latent Loss Function $\mathcal{L}_z$

In this section, we conduct an ablation study to assess the impact of different latent loss functions, $\mathcal{L}_z$. While our primary approach employs mean squared error (MSE) loss to directly align latent representation vectors, we also explore the use of cosine embedding loss: $\mathcal{L}_z = 1 - \cos(z_m^k, \hat{z}_m^j)$. For comparison, we consider the best results of each cases from Table 1 and Table 2. As summarized in Table 6, the performance remains consistent across both loss functions, with variations ranging from -0.1% to 0.3%. These results suggest that adhering to the representation distribution of the M_j modality effectively supports the training of the M_i modality, regardless of the choice of loss function.

Table 6: Performance comparison of different $\mathcal{L}_z$ across various datasets and cases

	MSE	**Cosine Embedding Loss**
ImageNet-1K **[L→V]**	79.54	79.61 (+ 0.07)
IEMOCAP **[L→A]**	61.29	61.20 (− 0.09)
IEMOCAP **[A→L]**	56.45	56.77 (+ 0.32)
AVMNIST **[V→A]**	42.44	42.67 (+ 0.23)
AVMNIST **[A→V]**	66.56	66.25 (− 0.31)

C.2 Additional results in larger Model

We also conducted experiments with a larger model, focusing on the **[L→V]** case on the ImageNet-1k dataset. Specifically, we utilized ViT-L/16, which requires approximately 5× more FLOPs compared to ViT-B/16. As the results are provied on Table 7, it demonstrate that our approach achieves significant improvements even with this larger model. This indicates that our method does not rely on the scalability of model size; instead, it leverages the qualitative representations of the M_j modality to effectively synergize with or enhance the training of the M_i modality.

Table 7: Large model classification results on ImageNet-1K and evaluation benchmarks

Model [L→V]	**IN**	**V2**	**Rend.**	**Sketch**	**A**	**Style.**	**C** (↓)
ViT-L/16 (reproduced)	78.31	68.99	49.03	37.88	29.14	23.25	46.39
+ RoBERTa (Liu et al., 2019)	80.71	70.62	52.50	40.45	31.85	27.47	41.61